2008-01

Charateristics of the transition from grain-boundary sliding to solute drag creep in superplastic AA5083

McNelley, Terry R.; Oh-Ishi, Keiichiro; Zhilyaev, Alexander P.; Swaminathan, Srinivasan; Krajewski, Paul E.; Taleff, Eric M.

Elsevier

T.R. McNelley, K. Oh-Ishi, A.P. Zhilyaev, S. Swaminathan, P.E. Krajewski, E.M. Taleff, "Characteristics of the transition from grain-boundary sliding to solute drag creep in superplastic AA5083," Metallurgical and Materials Transactions A, v.39A (January 2008), pp. 50-64.

http://hdl.handle.net/10945/55869

Characteristics of the Transition from Grain-Boundary Sliding to Solute Drag Creep in Superplastic AA5083

TERRY R. McNELLEY, KEIICHIRO OH-ISHI, ALEXANDER P. ZHILYAEV, SRINIVASAN SWAMINATHAN, PAUL E. KRAJEWSKI, and ERIC M. TALEFF

Superplastic tensile ductility has been attained when specially-processed AA5083 materials are strained in tension at relatively high strain rates, in the range of the transition from grain-boundary sliding (GBS) to solute drag creep (SDC) control of deformation. Quick plastic forming (QPF) technology involves deformation at such strain rates, and the relative contributions of GBS and SDC to the strain during deformation in this strain rate regime have been examined in this investigation. The additive, independent contributions of GBS and SDC to the elevated temperature deformation of fine-grained materials are reviewed. The transition from GBS to SDC in grain-refined AA5083 materials was evaluated by several methods, including the assessment of initial transients during straining and of transients during strain-rate change tests; the strain-rate dependence of the flow stress; the dependence of ductility on strain rate; flow localization behavior and fracture mode; cavitation growth; the evolution of microstructure and microtexture during deformation; and comparison with phenomenological models for the GBS-to-SDC transition.

DOI: 10.1007/s11661-007-9401-5

I. INTRODUCTION

INCREASING the use of aluminum in automobiles can contribute to reduced mass and, thereby, improve vehicle fuel economy and performance. However, the relatively low formability of aluminum alloys in conventional stamping operations is an impediment to the expanded use of aluminum in vehicle applications.[1,2] The superplastic forming (SPF) of aluminum sheet materials offers an alternative approach, but optimum superplastic ductility generally requires deformation at the slow strain rates of the grain-boundary sliding (GBS) regime. This limitation generally precludes the use of conventional SPF techniques for the high-rate production of vehicle components.[2–5]

Quick plastic forming (QPF) technology is a proprietary variation on SPF and involves the hot blow forming of aluminum alloys, such as fine-grained AA5083, at higher rates and lower temperatures than are employed in conventional SPF.[3,5] During QPF, deformation takes place in a regime of strain rate and temperature in which both GBS and solute drag creep (SDC) contribute together.[6–8] For the deformation of Al-Mg alloys such as AA5083 in the combined GBS and SDC regime, values of the strain-rate sensitivity coefficient, $m \equiv d\log\sigma/d\log\dot{\varepsilon}$, of 0.25 through 0.33 were reported, where σ is the true flow stress and $\dot{\varepsilon}$ is the true strain rate.[6] In general, slip creep processes involving diffusion-controlled dislocation climb in coarse-grained polycrystalline materials give $m \simeq 0.2$[9,10] and ductility ≤ 100 pct.[11,12] Resistance to localized necking and ductility increase as m values increase, and so the strain-rate sensitivity coefficients observed in AA5083 during deformation in the combined GBS and SDC regime may facilitate QPF. A more complete understanding of GBS and solute-drag-controlled slip creep during deformation in the transition regime will facilitate the broader application of the QPF of aluminum alloys.

Conventional SPF relies on the capability of fine-grained materials to undergo large, neck-free tensile elongations prior to failure during deformation at temperatures and strain rates at which GBS is the predominant deformation mechanism.[13–22] Forming temperatures are typically $\geq 0.5T_M$, where T_M is the melting temperature, and the time-temperature dependence of superplasticity is similar to that for creep deformation. The microstructure prerequisites for superplasticity include fine grains and grain boundaries that can sustain GBS while resisting tensile separation. Deformation by GBS is associated with $m \geq 0.5$, and fine-grained superplastic materials typically exhibit tensile ductility ≥ 200 pct.

The elevated-temperature constitutive behavior of fine-grained superplastic materials has been described in terms of the independent, additive contributions of

TERRY R. McNELLEY, Professor, and SRINIVASAN SWAMINATHAN, NRC Postdoctoral Associate, are with the Center for Materials Science and Engineering, Department of Mechanical and Astronautical Engineering, Naval Post Graduate School, Monterey, CA 93943-5146, USA. KEIICHIRO OH-ISHI, Postdoctoral Fellow, is with the National Institute for Materials Science, Tsukuba, Ibaraki 305-0047, Japan. ALEXANDER P. ZHILYAEV, RyC Research Associate, is with the Department of Physical Metallurgy, Centro Nacional de Investigaciones Metallurgicas (CENIM), 28040 Madrid, Spain. PAUL E. KRAJEWSKI, Laboratory Group Manager, is with the Research and Development Center, General Motors Corporation, Warren, MI 48090-9056, USA. ERIC M. TALEFF, Professor, is with the Department of Mechanical Engineering, University of Texas at Austin, Austin, TX 78712-0292, USA. Contact e-mail: tmcnelley@nps.edu
Manuscript submitted May 24, 2007.
Article published online December 6, 2007

GBS and slip creep to the total deformation rate, $\dot{\varepsilon}_{\text{total}}$.[15,18,20] That is,

$$\dot{\varepsilon}_{\text{total}} = \dot{\varepsilon}_{\text{GBS}} + \dot{\varepsilon}_{\perp} \quad [1]$$

where $\dot{\varepsilon}_{\text{GBS}}$ and $\dot{\varepsilon}_{\perp}$ are the contributions from GBS and slip creep, respectively. This assumes that GBS and its accommodation processes take place in the grain boundaries and in an adjacent, mantlelike region of the grains, so that the contribution of GBS to the total strain rate increases as grain size decreases.[23] In contrast, slip processes occur within the grain cores, and so the slip creep rate is independent of grain size.[18,20,21]

According to Eq. [1], the faster mechanism will control the total deformation rate when independent processes contribute to deformation. Thus, at low applied stress, GBS, with $m \simeq 0.5$, will tend to exhibit a higher strain rate than slip creep, for which $m \simeq 0.2$ to 0.33, depending on the specific slip creep mechanism. Then, as the applied stress increases, a transition to control by slip creep may occur as the strain rate for this mechanism exceeds that for GBS. The strain-rate sensitivity coefficient for slip creep by lattice-diffusion-controlled climb in pure metals and many solid-solution alloys corresponds to a stress exponent value of $n \equiv 1/m \simeq 5$,[9,10] while strain-rate sensitivity coefficient values of $m \simeq 0.33$ ($n \simeq 3$) reflect SDC in binary Al-Mg alloys.[24–28] However, the addition of Mn to Al-Mg materials has been shown to alter alloy constitutive behavior, in that ternary Al-Mg-Mn compositions exhibit lower strain-rate sensitivity coefficient values of $m \simeq 0.25$ ($n \simeq 4$) as Mn content increases above approximately 0.25 wt pct.[29–33] Nevertheless, the persistence of inverse stress transients following strain-rate changes in the ternary Al-Mg-Mn alloys demonstrates that they still deform by SDC. Inverse stress transients involve an abrupt stress increase upon a step increase in strain rate, followed by a subsequent decay toward a relatively steady stress at the new strain rate. Thus, the m values reported for AA5083 may reflect the effect of the Mn on strain-rate sensitivity coefficients, and inverse stress transients that were also observed in the commercial AA5083 materials confirm that these alloys deform by SDC at high strain rates in this temperature regime.[6]

For the GBS regime, theory suggests that $\dot{\varepsilon}_{\text{GBS}} \propto 1/d^p$, where d is the grain size and $p = 2$ to 3.[12] Data indicate that the higher values of p in this range may be associated with grain-boundary diffusion and the lower values with lattice diffusion. In contrast, the activation energy for deformation will be equal to that for either climb or solute diffusion, for slip creep control of deformation at higher strain rates, where $\dot{\varepsilon}_{\perp}$ is independent of grain size. Thus, grain refinement will increase the range of strain rates and decrease the temperatures for GBS, and this is the basis for the requirement that $d \leq 10\mu$m, for a useful superplastic response in Al alloys.[18,20,21]

The details of the production practice for superplastic-grade AA5083 have been given previously.[6] The final stage of deformation processing to produce fine-grain, superplastic microstructures in AA5083 involves cold-rolling reductions of up to 80 pct, to obtain a sheet 1.2 to 1.6 mm in thickness. Heating of the sheet prior to forming produces a fine recrystallized microstructure. Grain size measurements in the undeformed grip sections of the tensile samples revealed the formation of equiaxed grains < 10 μm in size by recrystallization, when such sheet material is heated at 450 °C prior to QPF at this temperature. For these materials, an analysis of the tensile strain-rate change test data over a range of temperatures (425 °C through 500 °C) showed that $m \simeq 0.5$ at low strain rates ($\sim 10^{-5}$ s^{-1}), and that the apparent activation energy for deformation, $Q_{\text{app}} \simeq 100$ to 110 kJ/mol; apparent activation energies were determined according to $Q_{\text{app}} \equiv -R(\partial \ln \dot{\varepsilon}/\partial 1/T)_{\sigma/E}$.[6] This value of the activation energy for GBS is intermediate to the values of the activation energies for self diffusion[34] and grain-boundary diffusion in binary Al-Mg alloys,[21,35,36] suggesting that both processes contribute in this regime. A gradual transition in behavior was apparent in the data for all of the materials examined, and the analysis revealed that $m \simeq 0.25$ at higher strain rates ($\sim 10^{-2}$ s^{-1}), while the activation energy $Q_{\text{app}} \simeq 136$ kJ/mol. The latter value is the same as the activation energy for Mg solute diffusion in aluminum ($Q_{\text{solute}} \simeq 136$ kJ/mol).[37–39]

The observed strain rate-temperature dependence of deformation in fine-grained, superplastic AA5083 is consistent with GBS control at low strain rates and high temperatures, and with a gradual transition over one to two orders of magnitude in strain rate with the onset of SDC control at high strain rates and low temperatures. In related work, failure occurred by cavitation and cavity linkage after deformation by GBS, while flow localization accompanied cavity linkage in the SDC regime.[41,42] Other characteristics of superplastic deformation by GBS include the disruption and randomization of preexisting textures, equiaxed grains, and dynamic grain growth.[12,16,21] Few studies have examined texture evolution during SDC at elevated temperature. The development of a weak two-component fiber texture in recrystallized SKY5083 material (a low Si + Fe version of 5083) deformed in tension at $\dot{\varepsilon} = 10^{-1}$s^{-1}, and 535 °C has been reported.[41,42]

Four QPF-grade AA5083 sheet materials were examined in the present investigation. The aim of the investigation was to apply various characterization tools, including mechanical testing, conventional imaging techniques that included quantitative determination of cavity fractions, and orientation imaging microscopy (OIM) methods, to the transition from GBS to SDC during elevated temperature deformation. The evolution of microstructure and microtexture from the as-received condition through deformation under QPF conditions to various strains was evaluated in terms of the operative transformation processes and deformation mechanisms.

II. EXPERIMENTAL

Composition data for the AA5083 sheet materials examined in this study are provided in Table I; these are

Table I. Cold-Rolling Strains and Composition Data (Weight Percent) for AA5083 Materials

Material	ε_{cr}	t, mm	Composition (Wt Pct)						
			Mg	Mn	Si	Fe	Cr	Cu	Al
DC-A	−1.3	1.4	4.71	0.86	0.09	0.21	0.10	0.04	bal
DC-B	−1.3	1.6	4.69	0.78	0.06	0.11	0.06	0.01	bal
DC-C	−1.3	1.3	4.50	0.76	0.15	0.20	0.07	0.03	bal
DC-D	−1.1; −1.4	1.6; 1.2	4.80	0.89	0.10	0.24	0.13	0.04	bal

the same materials as were examined in previous reports,[6,40] and the designations here are also the same as those given previously. All of these materials were produced by direct-chill casting, and further details of the processing of these commercial sheet materials have also been provided previously. The true strain values and sheet thicknesses associated with the final cold-rolling reductions are included for each material; these values correspond to reductions of 66 to 76 pct.

In the current study, static recrystallization behavior was examined by heating and annealing of 25 × 25-mm coupons that had been cut from the as-received sheet material. These were placed on a 12.7-mm-thick copper plate in a preheated box-type furnace set at the intended recrystallization temperature. Coupon temperature was monitored directly by a thermocouple, and the time at temperature was determined after the thermocouple indicated that the coupon was within 5 °C of the desired value. Annealing was conducted at 425 °C, 450 °C, 475 °C, 500 °C, or 535 °C, for times varying from 360 to 3600 seconds.

The details of tension testing procedures employed in evaluation of the strain-rate dependence of the flow stress have been described previously.[6,40] Briefly, strain-rate change tests were used, in which samples were initially deformed to a strain of ~0.15 and then subjected to a series of abrupt strain-rate changes, after successive strain intervals of ~0.03. Additional mechanical tests were conducted for the present investigation, using the DC-D material that had been cold rolled to a strain $\varepsilon_{CR} = -1.4$(76 pct reduction), while mechanical test data for the other materials have been taken from the previous investigations. The tension testing in the present study was conducted along the sheet-rolling direction at 450 °C, using constant nominal strain rates. Initially, a series of samples was strained to failure. Subsequent tests at selected strain rates were terminated at various strains prior to failure, in order to examine the strain dependence of microstructure, the cavitation growth behavior, and the evolution of microtexture. Details of the sample geometry for these tests have been given previously;[42] these were sheet-type coupons machined with tensile axes parallel to the sheet rolling direction, with gage dimensions of 12.7-mm length × 5.1-mm width × sheet thickness. The radius of curvature at the transition from the gage to the grip section was 1.6 mm. A split shoulder-grip design prevented deformation outside of the gage length. The tension testing was conducted using an Instron 4507 (Instron, Norwood, MA) electromechanical machine, and the test temperature was maintained constant to within ±2 °C, through the use of a five-zone, clamshell-design tubular furnace.

Sample preparation methods for optical microscopy and procedures for the quantitative determination of grain size and cavity volume fractions from micrographs have also been given previously.[6,40] During OIM, electron backscatter diffraction (EBSD) patterns form within about 30 nm of the sample surface.[43] Accordingly, the sample preparation for OIM involved mechanical polishing followed by electropolishing in a Buehler Electromet 4 apparatus (Buehler, Lake Bluff, IL), using a 20 pct perchloric acid/80 pct ethanol electrolyte cooled to −25 °C. The OIM used a Topcon S510 (Topcon Technologies, Inc., Paramus, NJ) scanning electron microscope (SEM) operating with a tungsten filament and the EDAX–TSL (AMETEK, Paoli, PA) OIM analysis package. The minimum step size of 0.1 μm was always ≤ 0.1 of the mean (sub)grain size in the recrystallized materials. The OIM study involved standard cleanup procedures,[43,44] as follows: (1) grain dilatation with a grain tolerance angle (GTA) of 5 deg, with a minimum grain size (MGS) of 2 pixels; (2) grain confidence index (CI) standardization, with GTA = 5 deg and MGS = 2; and (3) neighbor CI correlation, with minimum CI of 0.1. Data representations included grain maps, discrete pole figures, and grain-to-grain disorientation* distributions. The area-weighted average grain size option in the OIM software was used in the current investigation.** The mean-lineal-intercept grain size value may also be determined by the OIM software, or calculated from the area-weighted average using the equation $d_{AW} \simeq 1.728\ d_{\mathrm{mli}}$, where d_{AW} is the area-weighted average grain size and d_{mli} is the corresponding mean-lineal-intercept value.[45] Discrete pole figures were normalized and relative intensities were plotted as a function of the

*Disorientation refers to the minimum angle among all crystallographically-equivalent rotations that bring adjacent lattices into coincidence.

**During OIM, the electron beam is used as a point-by-point probe of lattice orientation; grains are formed by an algorithm that groups together sets of connected points having similar orientations within a tolerance. The area corresponding to each grain is determined from the pattern and spacing of these points; from these areas, the equivalent circle diameters are determined and the area-weighted average diameter is then calculated.

angle to the fiber axis. Peak intensity values were then evaluated as a function of strain, for samples deformed in uniaxial tension.

III. RESULTS

A. *Recrystallization of the As-Received Material*

The as-received AA5083 materials all exhibited distinct deformation textures, due to the cold rolling in the final stage of the processing. The B (or Brass) texture component ($\{110\}\langle 112\rangle$, where the notation refers to {plane parallel to the rolling plane} < direction parallel to the rolling direction >) was prominent in the orientation distribution functions calculated from OIM data, for all of the as-received materials. A representative set of discrete pole figures obtained for the as-received DC-B material are shown in Figure 1(a); in these data, RD is the rolling direction and TD the transverse direction, in the as-rolled sheet material. The B component is also apparent, when these are compared to standard projections for various rolling texture orientations.[46] The OIM grain map in Figure 1(b) was constructed from the discrete orientation measurements, and only those pixels

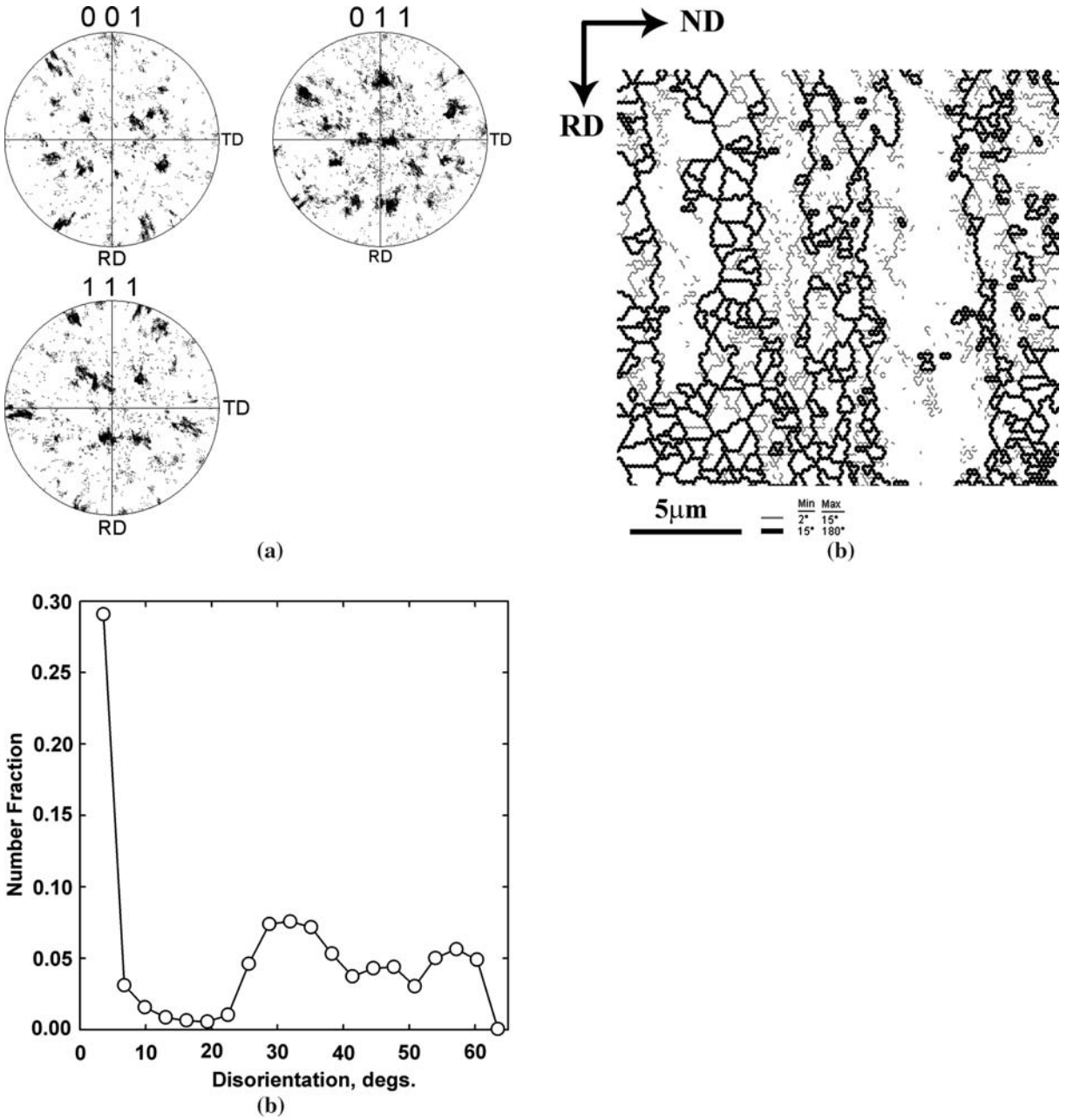

Fig. 1—OIM results for cold-rolled DC-B AA5083 material. Discrete 200, 220, and 111 pole figures show (*a*) a B-type rolling texture in as-rolled material, (*b*) an elongated deformation microstructure in the grain map, and (*c*) a high fraction of low-angle boundaries in the disorientation distribution.

corresponding to orientation differences of 2 through 15 deg (thin lines) or >15 deg (thick lines) are plotted. In this form, these data show elongated grains separated by high-angle boundaries and the presence of fine cells or subgrains within the grains. In some cases, the cell or subgrain boundaries exhibit disorientations >15 deg. The distribution of disorientation angles is shown in Figure 1(c); the microstructure comprises mainly low-angle boundaries.

The deformation texture of the as-received material was replaced by a nearly random texture within the initial 360 seconds of annealing at 450 °C. This may be seen in the discrete pole figures of Figure 2(a). These data were also obtained from the DC-B material and are, again, representative of results for all materials in this study. The distribution of orientations is largely random in Figure 2(a), but a weak cube component, $\{100\}\langle 001\rangle$, may also be discerned. Random textures identical to that in Figure 2(a) were observed at 360 seconds for all annealing temperatures investigated, and there were no further discernable changes in texture noted for anneals with durations up to 3600 seconds, for any of these materials. The transformation of the texture was accompanied by the formation of equiaxed grains, as illustrated in Figure 2(b). This OIM grain map was constructed in the same manner as the map in

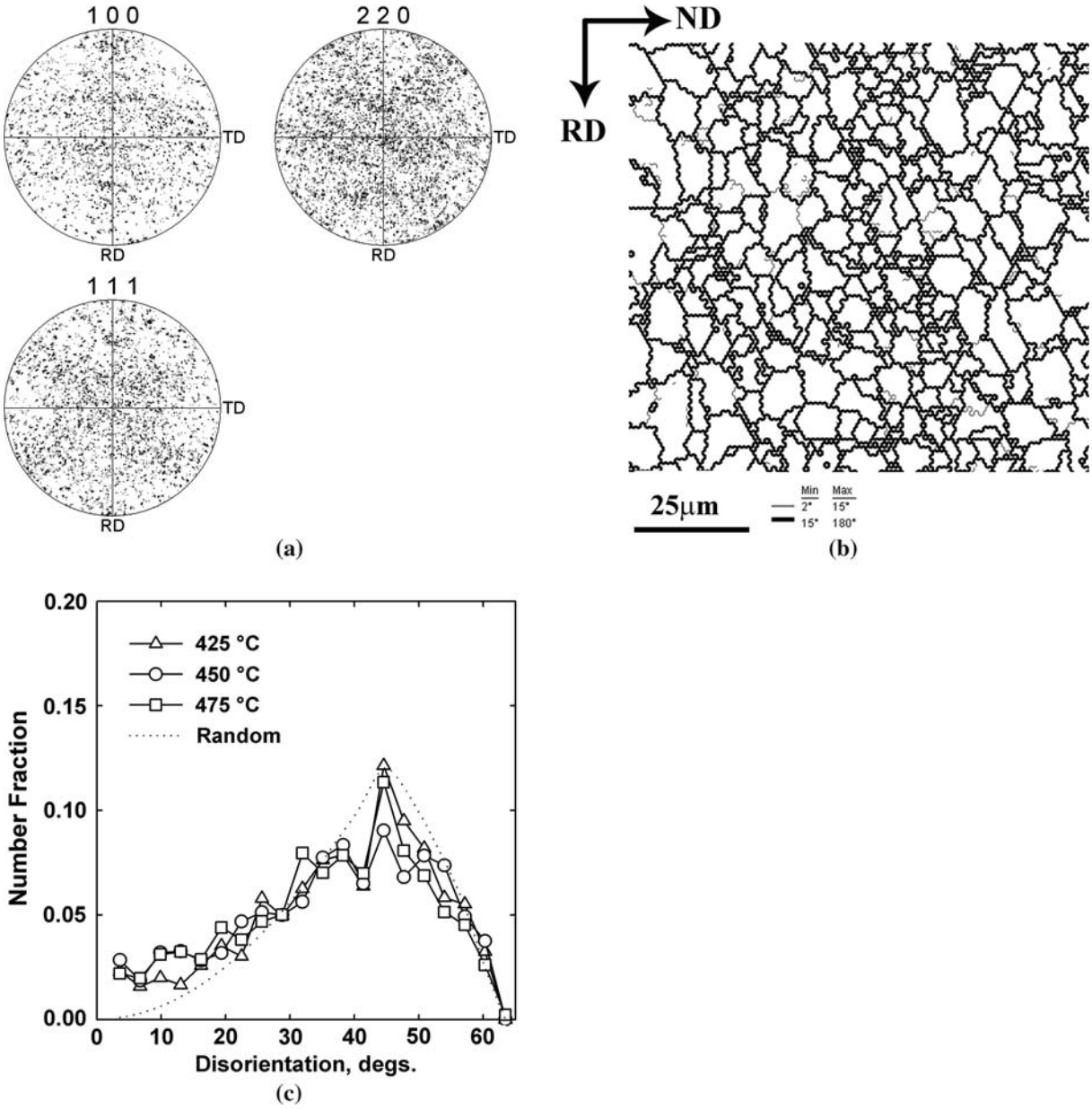

Fig. 2—OIM results for DC-B material after heating of cold-rolled material for 360 s at 450 °C. (*a*) Discrete 200, 220, and 111 pole figures show that the deformation texture of the cold-rolled material has been replaced by a nearly random texture. (*b*) Grain map indicates that the elongated structure of the cold-rolled material has been replaced by equiaxed grains. (*c*) Disorientation distributions similar to the Mackenzie random distribution[47] and showing the predominance of high-angle boundaries in the microstructure.

Figure 1(b) (note the difference in magnification), and consists mainly of thick lines that outline approximately equiaxed grains in a microstructure that comprises mainly high-angle boundaries. Grain-to-grain disorientation distributions for the DC-D material are plotted in Figure 2(c). These are representative of all of the distributions observed after recrystallization anneals. These distributions correspond to the Mackenzie disorientation distribution[47] for randomly-oriented cubes (shown by the dotted line in Figure 2(c)), although the population of low-angle boundaries (≤5 deg) exceeds that for a random material and reflects the presence of subgrains after recrystallization.

Area-weighted average grain size data for annealing of the DC-D materials that had been cold rolled to either 66 or 76 pct reduction are included in Figure 3(a), while the effect of annealing temperature on grain size is shown in Figure 3(b). Altogether, these data indicated that formation of refined, equiaxed grains by recrystallization of the cold-rolled materials is complete within 360 seconds. These grains have randomly-distributed lattice orientations and random grain-to-grain disorientations. The recrystallized grain size increases gradually from 6 to 7 μm after annealing at 425 °C, to ~8 μm following annealing 500 °C. When this AA5083 material is annealed at 535 °C, which is the temperature for conventional SPF of the SKY5083 material, grain growth results in an apparent grain size of 10 to 12 μm, and this is approximately the same grain size that is reported for the SKY material.[42] Mean-lineal-intercept grain sizes were calculated from the OIM area-weighted grain diameters, as described in Section II, and the results are compared in Table II to conventional mean-lineal-intercept measurements made by optical microscopy methods for the same samples. It is apparent that the former values are significantly smaller than the latter values. Similar discrepancies between OIM and optical microscopy have been attributed to the different mechanisms for identifying grains in these techniques.[48]

In these AA5083 materials, the processing has resulted in fine, equiaxed, and stable grains and predominantly high-angle boundaries. Thus, upon heating prior to QPF, the microstructure meets the prerequisites for superplasticity. The contributions of GBS and SDC to the subsequent deformation will be examined in several ways. These include analysis of the stress-strain curves and the strain-rate dependence of the flow stress, flow localization behavior during deformation, the evolution of texture during straining, and the failure mechanisms that occur after GBS and SDC deformation.

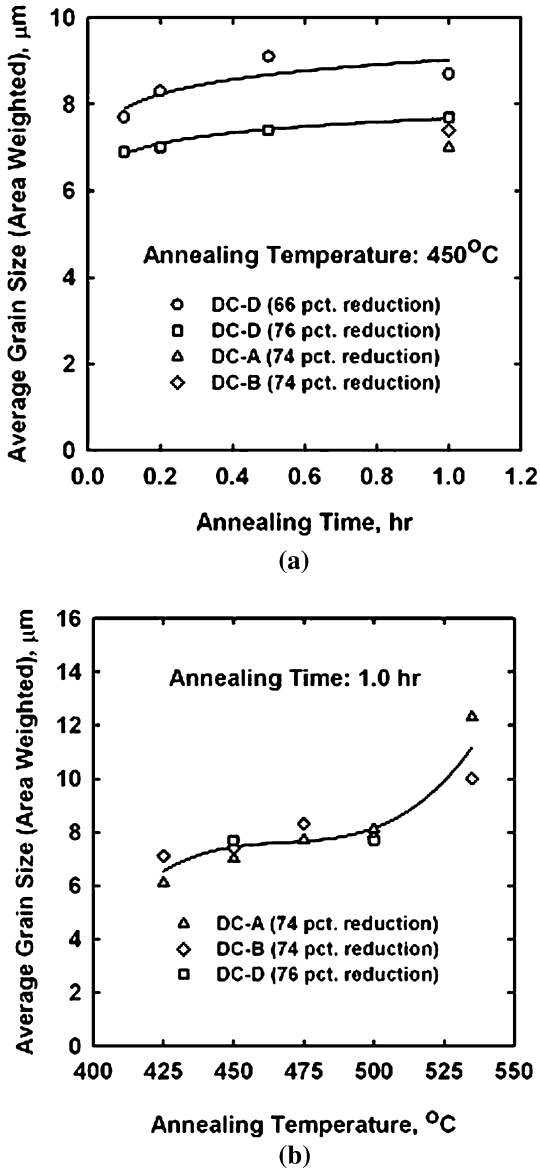

Fig. 3—(*a*) Recrystallized grain size (area-weighted average) is plotted as a function of annealing time at 450 °C, and shows that grain size is stable at this temperature; increased rolling reductions give a finer recrystallized grain size. (*b*) Recrystallized grain size increases gradually with increased annealing temperatures up to 500 °C.

B. *Tension-Testing Results*

Stress-strain curves of the DC-D were calculated from load-elongation data, using the standard definitions of true stress and strain, and the results are shown in Figure 4 for the tension tests conducted at 450 °C. Each of these samples was strained to failure at a constant nominal strain rate. The flow curves exhibit an initial stress transient for deformation at strain rates $\geq 10^{-2}$ s^{-1}, while this transient is absent at lower strain rates. In Figure 5(a), the true flow stress at a strain of 0.1 is plotted as a function of the strain rate on double logarithmic axes; here, the data were fitted with a spline function, to provide a smooth curve. The flow stress at a strain of 0.1 may not reflect equilibrium conditions at the highest strain rates, due to the effects of the transient as well as the onset of flow localization. The corresponding ductility as a percentage elongation to failure is plotted as a function of the strain rate, in Figure 5(b). Strain-rate sensitivity coefficient values were estimated from the data of Figure 5(a), by applying the relationship $m = \Delta \log \sigma / \Delta \log \dot{\varepsilon}$ to successive pairs of points, and the corresponding variation in the m value with the strain rate is also included in Figure 5(b). These data show that the value of m decreases from a maximum ~0.45 at a strain rate of ~5×10^{-4} s^{-1}, corresponding to

Table II. Comparison of Grain Size Determined by OIM and by Optical Microscopy

Material	Area Weighted Grain Size (OIM), μm	Calculated Mean Lineal Intercept (from OIM), μm	Mean Lineal Intercept (Optical), μm[6]
DC-A	7.2	4.2	6.9
DC-B	7.5	4.3	6.6
DC-D (1.6 mm)	8.4	4.9	8.2
DC-D (1.2 mm)	7.1	4.1	7.0

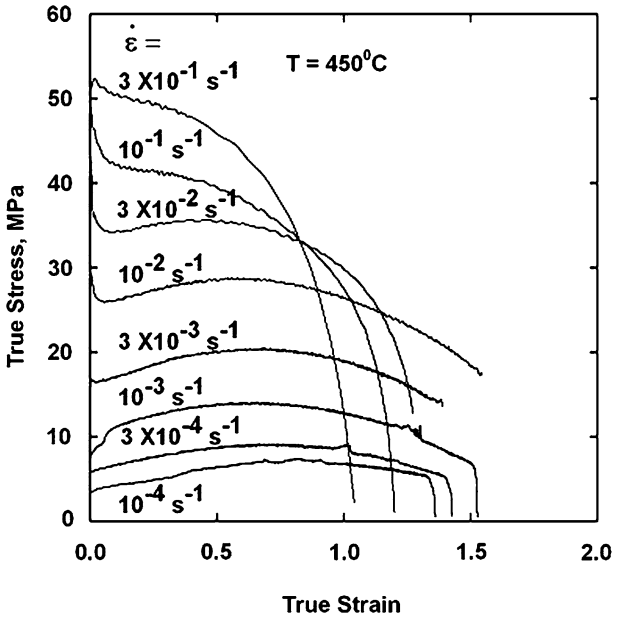

Fig. 4—Stress as a function of strain (true definitions) for tension testing at various nominal strain rates at 450 °C. An initial stress transient for strain rates $\geq 10^{-2}$ s^{-1} is consistent with SDC. The disappearance of this transient at lower strain rates is consistent with a transition to GBS control of deformation.

deformation by GBS, to ≤0.25 at a strain rate of $\sim 5 \times 10^{-2}$ s^{-1}, and deformation by SDC. The combination of flow stress and strain rate for the highest strain rate test here corresponds to the onset of power law breakdown (PLB) for binary Al-Mg alloys,[28,31–33] and this is reflected in an apparent m value < 0.25.

The elongation to failure data in Figure 5(b) exhibits a broad peak with elongations of 290 to 380 pct at strain rates up to 10^{-2} s^{-1}. The highest ductility corresponds to an intermediate value of the strain rate sensitivity, $m \simeq 0.35$, at 10^{-2} s^{-1}, which appears to be well into the regime of the transition from GBS to SDC. Furthermore, superplastic tensile ductility (> 200 pct elongation) persists at strain rates up to 3×10^{-2} s^{-1}. Together, the strain-rate dependence of the elongation and the rate sensitivity reflect the contributions of SDC as well as GBS to superplastic ductility.

A measure of the degree of flow localization during tension testing to failure has been defined in terms of the observed reduction in area at the point of failure, q, and the theoretical reduction in area, q,* that would occur in the absence of flow localization.[40,49] From this definition,

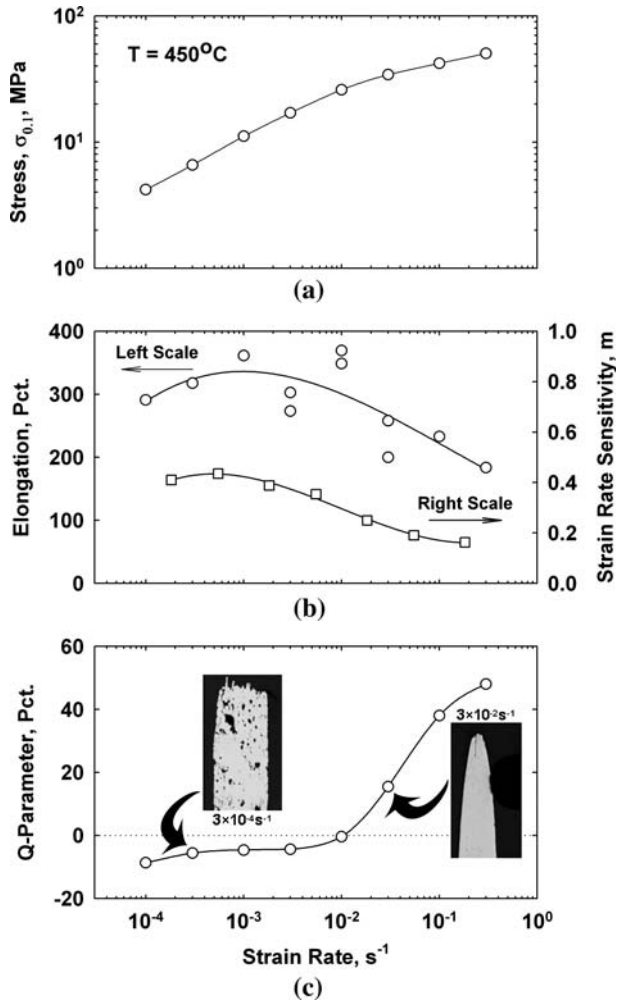

Fig. 5—(*a*) Plot showing the flow stress at a strain of 0.1 as a function of the nominal strain rate. (*b*) The corresponding m value and ductility data indicate a change in deformation mechanism at a strain rate of $\sim 10^{-2}$ s^{-1}; peak ductility is observed at a strain rate at which m ≈ 0.35. (*c*) The variation of the Q parameter with strain rate shows that cavitation is extensive in the GBS regime, while reduced rates of cavitation growth and flow localization predominate in the SDC regime.

$$q^* = \left(1 - \frac{1}{1 + e_f}\right) \quad [2]$$

where e_f is the elongation to failure. Then, a parameter, Q, can be defined as

$$Q = \frac{q - q^*}{q^*} \quad [3]$$

A positive value of the Q parameter indicates that flow localization, or necking, has occurred during the tension test. A Q parameter value of zero corresponds to extension and failure without necking, while a negative value of this parameter indicates macroscopic dilatation through cavitation during deformation. Reduction-in-area and elongation-to-failure measurements were used to calculate values of the Q parameter (as percentages) for the test series of Figure 4, and the resulting values are plotted as a function of strain rate in Figure 5(c). Profile views of the fractures for the samples deformed at 3×10^{-4} s^{-1} and 3×10^{-2} s^{-1} are shown in the low-magnification micrographs inset into Figure 5(c). Negative values of the Q parameter correspond to the absence of flow localization and cavitation for deformation at slow strain rates in the superplastic regime. In contrast, it is apparent that flow localization due to necking occurred in the sample deformed at higher strain rates, as well as less cavitation. In this form, the data indicate that flow localization occurred only at strain rates $> 3 \times 10^{-2}$ s^{-1}, where $m \simeq 0.25$, and that dilatation in the absence of flow localization occurred at strain rates $\leq 3 \times 10^{-3}$ s^{-1}, where $m \simeq 0.37$ to $\simeq 0.45$.

C. *Cavitation*

A series of interrupted tension tests was conducted at 450 °C and nominal strain rates of either 3×10^{-4} s^{-1} or 3×10^{-2} s^{-1}; the details of these tests are provided in Table III. Optical micrographs illustrating the evolution of cavitation with strain for these samples are shown in Figure 6(a). Elongated cavities that have apparently formed in association with stringers of constituent particles are evident in the samples deformed at 3×10^{-2} s^{-1}, at which SDC contributes significantly to the overall deformation. In contrast, irregularly-shaped cavities have formed in the samples deformed in the GBS regime. The cavity volume fractions were determined for each of these samples, and the results are summarized in Table IV and in Figure 6(b), along with data from previous work on cavitation growth in these AA5083 materials. The dependence of the cavity volume fraction on strain during plasticity-controlled cavity growth at elevated temperatures has been described by the relationship $V_c = V_0 \exp(\eta\varepsilon)$, where V_c is the volume fraction of cavities, V_0 and η are constants, and ε is the strain.[40,50–52] Accordingly, the volume fraction of cavities in Figure 6(b) is plotted as a function of the strain on semilogarithmic coordinates. These data show clearly that cavitation growth rates, as reflected in the coefficient η, are greater at lower strain rates in the GBS regime than at higher strain rates in the transition regime.

D. *Texture Evolution*

The deformation and flow localization results are consistent with a transition in deformation mechanism centered at a strain rate of ~10^{-2} s^{-1}. Thus, the samples from the interrupted tension tests at strain rates of either 3×10^{-2} s^{-1} or 3×10^{-4} s^{-1} and at 450 °C were also examined by OIM methods. The test conditions and strain values were given in Table III. Discrete pole figure data acquired from the samples deformed in the GBS regime are shown in Figure 7(a). The RD in the pole figures is the prior rolling direction, and this is also the direction of the tensile axis. These pole figures exhibit random textures and a comparison of these results with the data for the annealed condition in Figure 2(a) reveals no significant change in the texture from the annealed condition during deformation. Corresponding discrete pole figures in Figure 7(b) for the samples deformed in the SDC regime indicate the progressive development of a two-component $\langle 100 \rangle + \langle 111 \rangle$ fiber texture, which strengthens during deformation. The notation is < direction aligned with the fiber axis > and inspection of the data in Figure 7(b) shows that the fiber axis is aligned with the tensile axis (*i.e.*, the RD). These data were analyzed as fiber textures to determine the relative intensity, I/I_0, where I is the intensity and I_0 is the intensity expected from a random sample, as a function of angle to the fiber axis, for both the $\langle 100 \rangle$ and $\langle 111 \rangle$ poles. The peak intensity along the fiber axis was determined from this analysis and is plotted in Figure 8 as a function of the local true strain (at the location of the texture analysis), for this series of samples. The plot in Figure 8(a) shows the relative intensity for the $\langle 111 \rangle$ component as a function of strain for the GBS and SDC samples, while corresponding data for the $\langle 100 \rangle$ are presented in Figure 8(b). These results show that the relative intensity remains unchanged during deformation in the GBS regime, while both the $\langle 100 \rangle$ and $\langle 111 \rangle$ fiber texture components strengthen approximately linearly with strain.

Grain-to-grain disorientation distributions corresponding to the data of Figures 7 and 8 are shown in

Table III. Strains for the Interrupted Tension Tests in the Cavitation Study

High-Strain-Rate Series 3×10^{-2} s^{-1}		Low-Strain-Rate Series 3×10^{-4} s^{-1}	
El (Pct)	Local True Strain, ε_l*	El (Pct)	Local True Strain, ε_l*
103	0.55	93	0.51
201	1.05	200	0.88
226	1.32	245	0.99
258	1.80	318	1.28

*$\varepsilon_l = -\{\ln (W_i/W_0) + \ln (t_i/t_0)\}$.

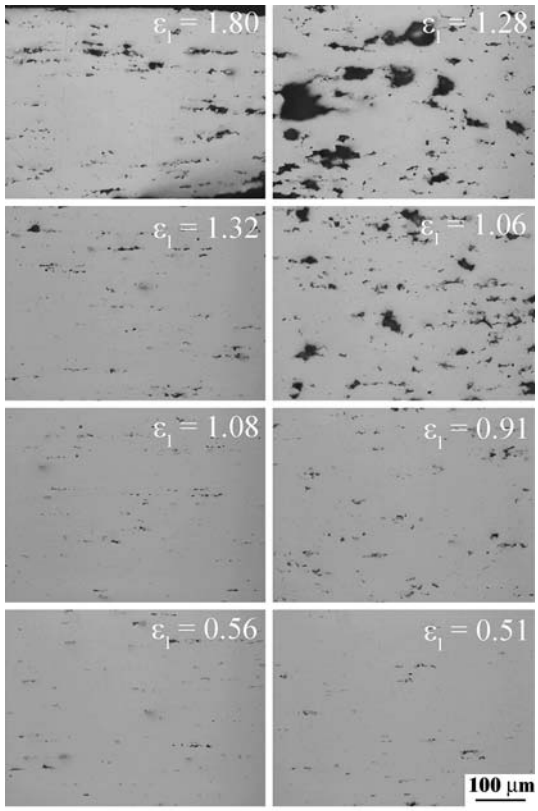

Fig. 6—(*a*) Optical micrographs from the interrupted tension testing (Table III) show the increase in area fraction of cavitation with strain under SDC conditions at a 3×10^{-2} s^{-1} strain rate, and under GBS conditions at 3×10^{-4} s^{-1}. (*b*) Exponential dependence of the area fraction of cavitation on strain. The cavitation growth rate is higher when GBS controls deformation.

Figure 9. Also, Figure 9 includes OIM grain maps for samples that had been deformed to approximately 200 pct elongation in each of these regimes. The disorientation distributions are essentially unchanged from the annealed condition during GBS, as shown in Figure 9(a), although an increased population of low-angle boundaries is apparent in the sample deformed to failure. The development of low-angle boundaries near the failure strain during GBS may reflect a contribution from SDC, due to increased local stresses (and strain rates) in the ligaments in between cavities. A comparison of Figure 9(b) to Figures 2(b) and 3(a) reveals that the grain size exhibits dynamic growth during straining; grain elongation and the presence of low-angle boundaries may also reflect a contribution from SDC at this strain rate. In contrast, Figure 9(c) shows that the population of low-angle boundaries is approximately constant, from 103 to 258 pct elongation during straining in the SDC regime. This is consistent with subgrain formation during deformation at a near-steady-state condition. Grain elongation that is accompanied by the formation of low-angle boundaries is apparent in the OIM grain map in Figure 9(d). The formation of a deformation-induced two-component fiber texture, grain elongation, and development of a constant fraction of low-angle boundaries are consistent with a predominance of slip during steady-state deformation in the SDC regime.

IV. DISCUSSION

In this investigation, microstructure and microtexture analysis by OIM has shown that the deformation microstructures and textures in cold-rolled AA5083 materials, shown in Figure 1, are replaced by fine, equiaxed grains and random textures following brief anneals at typical QPF temperatures, as illustrated in Figure 2. The development of random textures during static annealing is consistent with particle-stimulated nucleation (PSN) of recrystallization.[53] This reaction involves the formation of new grains from fine, highly-disorientated cells or subgrains that developed within the deformation zones formed around dispersed particles during the prior cold working. The extent of the deformation zones scales with the particle size. Therefore, a dispersed particle must exceed a size of ~0.5 to 1.0 μm, so that a stable grain nucleus can form from a cell or subgrain contained within its deformation zone and enable it to become a site for PSN. Then, random recrystallization textures reflect the random lattice reorientations associated with accommodation of the particles, as the zones form during the prior deformation. The uniformly-distributed constituent particles and dispersoids in these AA5083 materials range from 0.1 to 20 μm in size and, apparently, PSN can support the formation of grains 7 to 8 μm in size. The random grain-to-grain disorientation distributions reflect the random grain textures developed during the PSN reaction. Thus, these microstructures have formed by a discontinuous reaction, and they meet the requirements for superplasticity within 0.1 hour of annealing, *i.e.*, prior to the onset of straining. This is in contrast to microstructures that evolve during superplastic straining *via* a continuous recrystallization reaction. Characteristics of the continuous reaction include the retention of prior deformation textures and gradual

Table IV. Parameters in the Exponential Cavitation Growth Relationship

	3×10^{-2} s^{-1}		3×10^{-4} s^{-1}	
T = 450 °C	V_0 (Pct)	η	V_0 (Pct)	η
DC-A,C[40]	0.13	1.7	0.0084	5.4
DC-B[40]	0.22	1.7	0.027	5.4
DC-D	0.073	1.93	0.020	5.06

evolution of high-angle boundaries during superplastic straining.[54–63]

From Table II, the grain-size values determined by OIM in the current investigation appear to be consistently 40 pct finer than those measured by conventional optical microscopy methods[6] on the same samples. A discrepancy of the same magnitude has been documented in a careful analysis of grain sizes determined by OIM and optical microscopy methods applied to a low-carbon steel and also to an Al-Cu-Mg alloy.[48] In samples of these materials, microhardness indentations were employed to identify regions that were then examined by both OIM and optical microscopy. It was shown that numerous boundaries that had been identified by orientation differences in OIM were not revealed by conventional polishing and etching. The resolution of these discrepancies is the subject of ongoing research.

A strain-rate-dependent transition in the rate-controlling mechanism is apparent during the tension testing of this material at 450 °C. The tests documented in Figure 4 were conducted at constant nominal strain rates varying from 10^{-4} to 3×10^{-1} s^{-1}, *i.e.*, at a temperature and in a strain-rate regime corresponding to QPF conditions. At the higher strain rates in this regime, stress transients at the beginning of stress-strain tests, or after strain-rate changes, reflect deformation by the SDC mechanism. At 3×10^{-2} s^{-1}, the flow curve exhibits an initial stress transient that is followed by strain hardening. The stress transient is smaller at an initial strain rate of 10^{-2} s^{-1}, and still smaller at 3×10^{-3} s^{-1}. Finally, the initial transient is absent at strain rates of 10^{-3} s^{-1} and below, and strain hardening is apparent during plastic deformation. At low strain rates in this regime, the strain hardening reflects GBS-controlled deformation, in which the increased flow stress is a reflection of the $1/d^p$ dependence of the strain rate on grain size for this mechanism. Altogether, the data of Figure 4 are consistent with independent, additive contributions of SDC

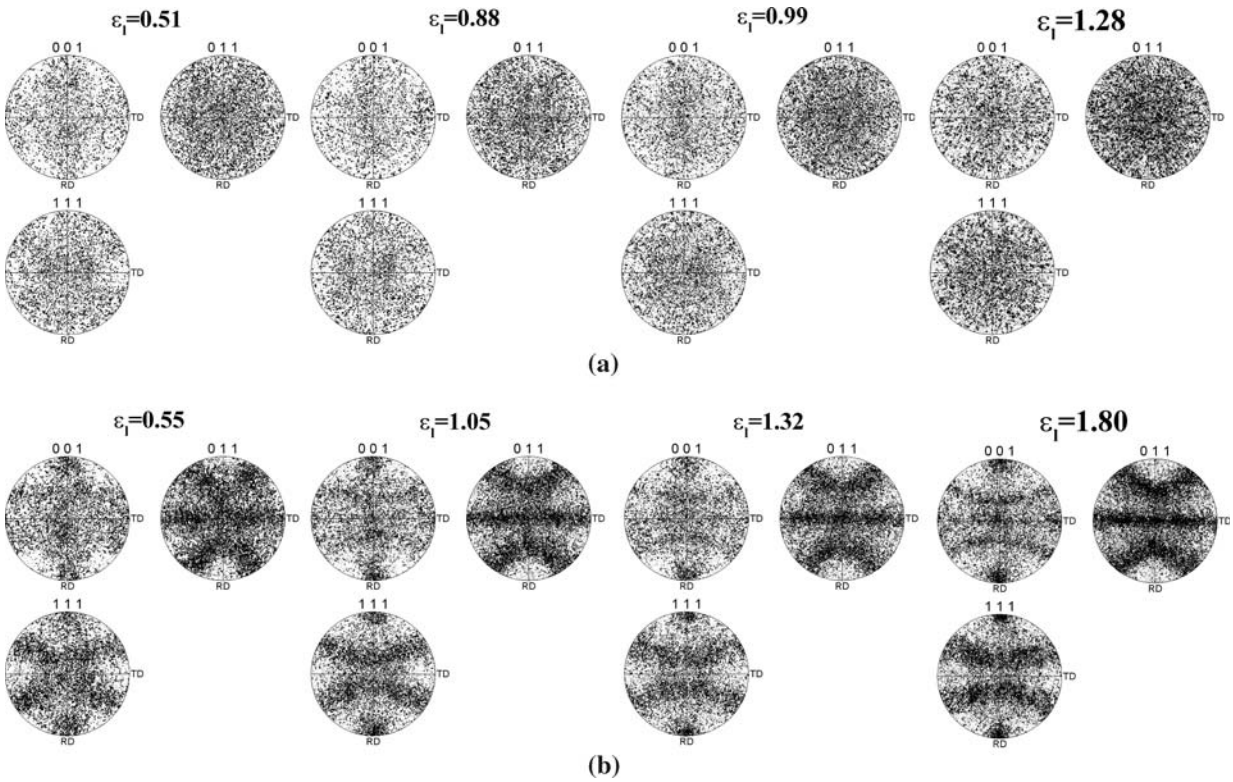

Fig. 7—(*a*) OIM microtexture data in the form of discrete 001, 011, and 111 pole figures for each sample in the series of Table II, showing the persistence of random textures during deformation under GBS control of deformation. (*b*) Development of a two-component ⟨100⟩ + ⟨111⟩ fiber texture due to SDC.

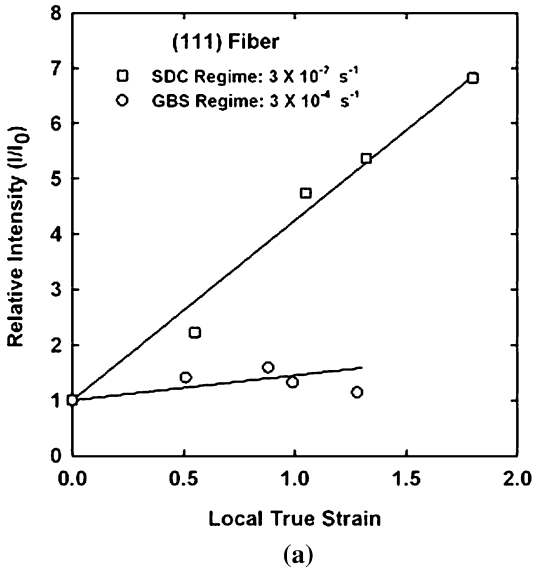

Fig. 8—Plots of relative intensity (I/I_0) as a function of true strain for the discrete pole figure data of Fig. 7 are shown for (*a*) the 111 fiber and (*b*) the 100 fiber in. Both fibers strengthen with strain under SDC conditions and remain random for GBS control of deformation.

and GBS to the deformation behavior, with SDC predominant at the highest strain rates and GBS at the lowest strain rates, and with a transition from SDC to GBS over about two orders of magnitude in strain rate, from ~10^{-1} s^{-1} downward to ~10^{-3} s^{-1}.

In Figure 5(b), the change in the strain-rate-sensitivity coefficient from $m \simeq 0.45$ to $m \leq 0.25$ as the strain rate increases from ~5×10^{-4} s^{-1} to ~5×10^{-2} s^{-1} is also consistent with a transition from GBS to SDC as well as with the onset of PLB at the highest rate in this interval of strain rates. The resistance to flow localization and necking increases as the strain-rate-sensitivity coefficient increases and, on this basis, the highest ductility would be expected to occur at a low strain rate in the GBS regime. However, high tensile ductility in this AA5083 material is observed to persist to a strain rate of 10^{-2} s^{-1}, where the strain-rate-sensitivity coefficient has decreased to a value of $m \simeq 0.35$. In Figure 5(c), negative Q-parameter values for strain rates $< 10^{-2}$ s^{-1} reflect dilatation due to cavitation growth, and so the ductility in the GBS regime is restricted by the formation, growth, and linkage of cavities more than by flow localization and necking. The highest ductility in this test series was observed at the strain rate where $Q = 0$ and ductility appears to depend on flow localization, as dictated by the material's strain-rate sensitivity, only at higher strain rates.

The data in Figure 6 show that the transition from GBS to SDC is also reflected in a transition in the cavitation growth rate, which apparently is greater for GBS control of deformation than for conditions involving large contributions of SDC to the deformation. Models for plasticity-controlled cavity growth[50,52] generally predict that cavity growth rates decrease, with a corresponding ductility increase, as the strain-rate-sensitivity coefficient increases, and data acquired under GBS-dominated deformation conditions[51] supports such modeling results. However, the data of Figure 6(b), in which cavitation growth rates are higher in the GBS regime than in the transition regime despite a higher strain-rate-sensitivity coefficient, contrast with these prior experimental and modeling results. This reflects that cavitation growth rates here were evaluated at a strain rate for which SDC is the predominant deformation mechanism. Furthermore, plasticity-controlled cavity growth models[50,52] neglect the role of constituent particles in processes of cavitation growth.[8,40] Altogether, these results confirm previous work indicating that there is a transition from GBS to SDC and an accompanying transition in failure mechanism during deformation in the QPF regime. Then, the tensile ductility during deformation in this regime reflects a balance of cavitation growth and flow localization. Here, this balance is reflected in the strain-rate dependence of the Q parameter.

The texture data in Figures 7 and 8 also delineate a transition from GBS to slip creep, and are consistent as well with a change in failure mechanism over this strain-rate regime. The random grain orientations of the recrystallized condition were retained during deformation in the GBS regime. Diffusion and slip processes involved in the accommodation of GBS take place in mantlelike regions near the grain boundaries,[23] and therefore do not produce lattice rotation and the development of preferred orientations in the texture. Instead, grains experience random rotations during GBS, resulting in the retention of the initially random texture. The blocking of sliding in the vicinity of grain triple junctions and constituent particles may result in the tensile separation of boundaries as a local accommodation mechanism during GBS, and thereby contribute to the initiation of cavitation. In contrast, during uniaxial deformation in the SDC regime, a distinct, two-component fiber texture forms from the random texture of the initial, recrystallized condition. The ⟨100⟩ and ⟨111⟩ components of the texture each have more than five active slip systems for tensile loading parallel to the

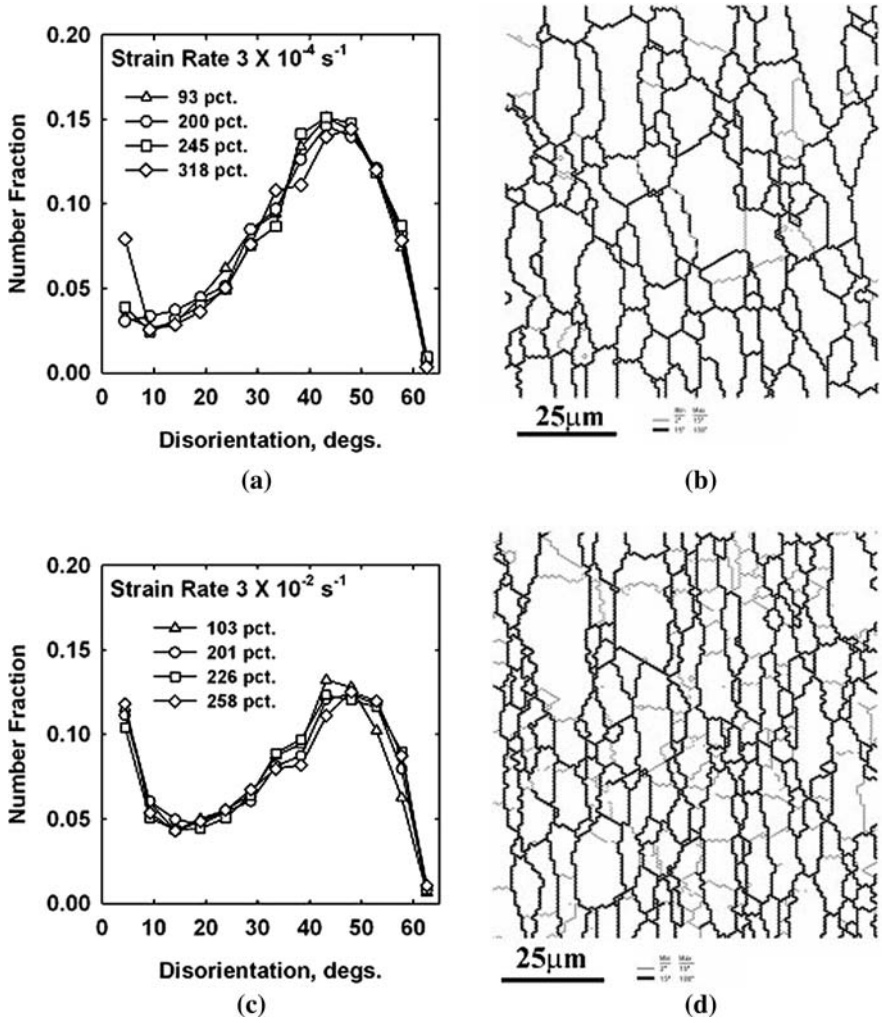

Fig. 9—(*a*) and (*b*) OIM disorientation distributions and grain maps for the sample series of Table III show the persistence of random grain-to-grain disorientation distributions and limited grain growth during straining under GBS conditions, respectively. (*c*) and (*d*) Development of low-angle boundaries and grain elongation taking place when SDC contributes to deformation, respectively.

fiber axis. Thus, grains having either orientation can deform compatibly with adjacent grains, as these fibers develop during uniaxial straining.[42] This, in turn, will reduce the need for local accommodation at grain boundaries, although not at nondeforming constituent particles. The latter will remain sites for cavity initiation, and this is apparent in the microscopy results in Figure 6(a). Again, the transition from GBS to SDC control of deformation in this AA5083 material is accompanied by a transition in failure mechanism. The peak ductility occurs at a strain rate in the transition region and reflects a balance of the lessened effects of cavitation growth and an increased tendency for strain localization as strain rate increases from the GBS regime to the SDC regime.

Phenomenological models were used with Eq. [1] to describe the GBS-to-slip-creep transition in SKY5083 for deformation at 535 °C.[42] At this temperature, the activation energy for deformation was close to that for lattice diffusion, and so the constitutive relationships for GBS and slip creep were simplified to include only lattice-diffusion terms. The analysis predicted the stress for the GBS to slip creep transition, but overestimated the strain rates, because of the use of a slip creep equation applicable to pure aluminum rather than to SDC in the alloy.

With appropriate phenomenological creep equations for GBS and SDC,[18] Eq. [1] becomes

$$\dot{\varepsilon}_{\text{total}} = A_1 \frac{D^*_{\text{eff}}}{d^2}\left(\frac{\sigma}{E}\right)^2 + A_2 D_{\text{solute}}\left(\frac{\sigma}{E}\right)^{n_{\text{SDC}}} \qquad [4]$$

where A_1 is a material-dependent constant for GBS, D^*_{eff} is a modified effective diffusion coefficient, d is the grain size, σ is the applied stress, and E is the dynamic, unrelaxed Young's modulus. In the second term, A_2 is a constant, D_{solute} is the solute diffusion coefficient (in the absence of data for the chemical interdiffusion coefficient, $\tilde{D}$) and n_{SDC} is the stress exponent for SDC. The second term in Eq. [4] may be written as $\dot{\varepsilon}_{\text{SDC}} = A_2 D_{0,\text{solute}} \exp(-Q_{\text{solute}}/RT)(\sigma/E)^{n_{\text{SDC}}}$, where $D_{0,\text{solute}}$ is the pre-exponential term in the diffusion coefficient. The product $A_2 D_{0,\text{solute}} \simeq 2.0$ to $8.0 \times 10^{20} \text{s}^{-1}$, when this

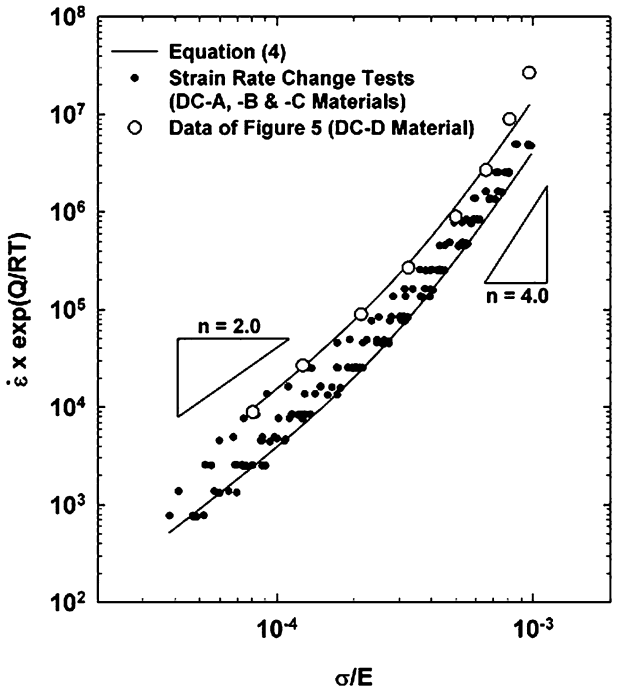

Fig. 10—Plots of the Zener–Hollomon parameter $\dot{\varepsilon}\exp(Q/RT)$ as a function of σ/E, with Q = 110 kJ/mol, for strain-rate-change data from DC-A, DC-B, and DC-C materials (closed symbols) and the DC-D material of the current investigation deformed at 450 °C. These data are compared to curves for Eq. [4], using values of A_1 and $A_2D_{0,sol}$ given in the text. The data for these AA5083 materials may be described in terms of the independent, additive contributions of GBS and SDC.

form is applied to the strain-rate-change test data for these AA5083 materials.[6] As noted earlier, $Q_{solute} \simeq 136$ kJ/mol and $n_{SDC} \simeq 4.0$.

The modified effective diffusion coefficient was shown to be given by[18]

$$D^*_{eff} \cong D_L + \frac{c\pi w}{d} D_{GB} \qquad [5]$$

where D_L is the lattice diffusion coefficient, c is a constant (~0.01 for many materials), w is the grain-boundary width (typically ≈ 2–$5b$, where **b** is the Burgers vector), and D_{GB} is the grain-boundary diffusion coefficient. The second term in Eq. [5] incorporates grain-boundary diffusion control of GBS. From the analysis of GBS in a broad range of materials, $A_1 \simeq 5 \times 10^7$ to 10^{10} and $A_1 \sim 2 \times 10^9$ were used in the analysis of the SKY5083 material. The lattice diffusion coefficient is $D_L = 1.7 \times 10^{-4}\exp(-Q_L/RT)$, $m^2\ s^{-1}$, with Q_L = 142 kJ/mol; likewise, the grain-boundary-diffusion coefficient is given by $D_{GB} = 5 \times 10^{-4}\exp(-Q_{GB}/RT)$, $m^2\ s^{-1}$, with Q_{GB} = 84 kJ/mol.[36]

The strain-rate-change test data that had been obtained for the DC-A, DC-B, and DC-C materials at temperatures from 425 °C through 500 °C were combined with the stress-strain test data for the DC-D material at 450 °C in the present study. The grain size was taken as 7.5 μm, and the results are summarized in Figure 10. In order to consolidate the data for both the GBS and SDC regimes onto a single plot, the strain-rate values for the DC-A, DC-B, and DC-C materials were represented by the Zener–Hollomon parameter $Z = \dot{\varepsilon}\exp(Q/RT)$, with Q = 110 kJ/mol, as a function of σ/E.[6] Two curves representing the strain rate as a function of σ/E were calculated using Eq. [4], and the results (after further adjustment by the Zener–Hollomon parameter) are included in Figure 10. For the upper curve, $A_1 = 6 \times 10^7$ and $A_2D_{0,solute} = 8 \times 10^{20}\ s^{-1}$; for the lower curve, $A_1 = 1.5 \times 10^7$ and $A_2D_{0,solute} = 2 \times 10^{20}\ s^{-1}$. Altogether, the data of Figure 10 show that the regime of the transition from GBS to SDC can be described by the independent, additive contributions of these mechanisms to the total deformation rate. The predicted and observed ranges of stress and strain rate over which the transition is predicted to occur agree well, as this is reflected in the apparent strain-rate dependence of the strain-rate sensitivity. The relative rates for GBS and SDC are consistent with the microstructure and microtexture measurements that indicate the predominance of GBS at lower rates (e.g., $3 \times 10^4\ s^{-1}$) and SDC at higher rates (e.g., $3 \times 10^{-2}\ s^{-1}$), and a transition over about two orders of magnitude in strain rate during deformation at 450 °C.

V. CONCLUSIONS

The following conclusions regarding the thermomechanical processing and elevated-temperature mechanical behavior of superplastic AA5083 materials have been reached as a result of this investigation.

1. The deformation-induced microstructure following cold working of the hot-band material to reductions of 67 through 80 pct includes a distinct B-type texture and cells and subgrains within elongated prior grains. Upon heating of this cold-worked material to typical QPF temperatures, superplastic microstructures form by the PSN of recrystallization, with the formation of refined, equiaxed grains 7 to 8 μm in size. The PSN reaction is discontinuous in nature and is accompanied by the formation of a random texture and random, high-angle boundaries that support superplastic response from the onset of deformation at 450 °C.
2. Stress-strain curves for the recrystallized material exhibit initial stress transients during deformation at 450 °C and strain rates $\geq 10^{-2}\ s^{-1}$, reflecting SDC control of deformation. The stress transient disappears at lower strain rates and the flow curves exhibit apparent strain hardening, consistent with dynamic grain growth during GBS.
3. The strain-rate-sensitivity coefficient, m, decreases in value from ~0.45 at a strain rate of $5 \times 10^{-4}\ s^1$ to ≤ 0.25 at $5 \times 10^{-2}\ s^{-1}$, while the tensile ductility exhibits a broad peak with a maximum value of 390 pct elongation to failure, at an intermediate strain rate of $10^{-2}\ s^{-1}$. The variation in m value is consistent with a transition from GBS to SDC over about two orders of magnitude in strain rate, and with the onset of PLB at the highest strain rate in the interval evaluated.

4. Cavitation growth rates in the GBS regime are higher than those for the SDC control of deformation. In the GBS regime, failure takes place by cavity growth and linkage; a transition in failure mechanism accompanies the transition from GBS to SDC, and failure is dominated by flow localization at higher strain rates.
5. The peak ductility in this superplastic AA5083 material is observed at a strain rate within the regime of the transition from GBS to SDC.
6. The random texture of the recrystallized condition is retained during deformation at the low strain rates of the GBS regime, reflecting random grain rotations that accompany sliding. Grains remain equiaxed and free of substructure during GBS. In contrast, a distinct two-component $\langle 111 \rangle + \langle 100 \rangle$ fiber texture forms during deformation at higher strain rates of the SDC regime. The onset of fiber texture formation is a marker for the change in the deformation mechanism. The SDC is also reflected in grain elongation and substructure formation.
7. Separate phenomenological creep models for the independent GBS and SDC deformation mechanisms may be adjusted and combined to predict the transition from GBS to SDC with increasing strain rate for QPF conditions. The combined model predicts a transition in the rate-controlling mechanism over approximately two orders of magnitude in strain rate, which is consistent with the range of the transition from flow characteristics, ductility data, failure mechanisms, and microstructure and microtexture observations.

REFERENCES

1. A. Kelkar, R. Roth, and J. Clark: *JOM*, 2001, vol. 53 (8), pp. 28–32.
2. P.A. Friedman and S.G. Luckey: *Mater. Sci. Forum*, 2003, vols. 447–448, pp. 199–204.
3. J.G. Schroth: in *Advances in Superplasticity and Superplastic Forming*, E.M. Taleff, P.A. Friedman, P.E. Krajewski, R.S. Mishra, and J.G. Schroth, eds., TMS, Warrendale, PA, 2004, pp. 9–10.
4. K. Osada and K Shirkawa: in *Advances in Superplasticity and Superplastic Forming*, E.M. Taleff, P.A. Friedman, P.E. Krajewski, R.S. Mishra, and J.G. Schroth, eds., TMS, Warrendale, PA, 2004, pp. 41–49.
5. P.E. Krajewski: in *Advances in Superplasticity and Superplastic Forming*, E.M. Taleff, P.A. Friedman, P.E. Krajewski, R.S. Mishra, and J.G. Schroth, eds., TMS, Warrendale, PA, 2004, pp. 173–83.
6. M.A. Kulas, W.P. Green, E.M. Taleff, P.E. Krajewski, and T.R. McNelley: *Metall. Mater. Trans. A*, 2005, vol. 36A, pp. 1249–61.
7. E.M. Taleff, W.P. Green, M.A. Kulas, T.R. McNelley, and P.E. Krajewski: *Mater. Sci. Eng. A*, 2005, vols. 410–411, pp. 32–37.
8. W.P. Green, M.A. Kulas, A. Niazi, K. Oh-ishi, E.M. Taleff P.E. Krajewski, and T.R. McNelley: *Metall. Mater. Trans. A*, 2006, vol. 37A, pp. 2727–38.
9. O.D. Sherby and P.M. Burke: *Progr. Mater. Sci.*, 1968, vol. 13, pp. 325–90.
10. M.E. Kassner and M.T. Pérez-Prado: *Fundamentals of Creep in Metals and Alloys*, Elsevier, Amsterdam, 2004, pp. 13–87.
11. D.A. Woodford: *Trans. ASM*, 1969, vol. 62, pp. 29–99.
12. T.G. Nieh, J. Wadsworth, and O.D. Sherby: *Superplasticity in Metals and Ceramics*, Cambridge University Press, Cambridge, United Kingdom, 1997, pp. 189–204.
13. T.G. Nieh, J. Wadsworth, and O.D. Sherby: *Superplasticity in Metals and Ceramics*, Cambridge University Press, Cambridge, United Kingdom, 1997, pp. 58–69.
14. A. Ball and M.M. Hutchison: *Met. Sci. J.*, 1969, vol. 3, pp. 1–7.
15. T.G. Langdon: *Metall. Trans. A*, 1982, vol. 13A, pp. 689–701.
16. J.W. Edington: *Metall. Trans. A*, 1982, vol. 13A, pp. 703–15.
17. A. Arieli and A.K. Mukherjee: *Metall. Trans. A*, 1982, vol. 13A, pp. 717–32.
18. O.D. Sherby and J. Wadsworth: in *Deformation Processing and Structure*, G. Kraus, ed., ASM, Metals Park, OH, 1984, pp. 355–87.
19. G.S. Murty and M.J. Koczak: *Mater. Sci. Eng.*, 1987, vol. 96, pp. 117–24.
20. O.A. Ruano and O.D. Sherby: *Rev. Phys. Appl.*, 1988, vol. 23, pp. 625–35.
21. O.D. Sherby and J. Wadsworth: *Progr. Mater. Sci.*, 1989, vol. 33, pp. 169–221.
22. T.G. Langdon: *Mater. Sci. Eng.*, 1991, vol. A137, pp. 1–11.
23. R.C. Gifkins: *Metall. Trans. A*, 1976, vol. 7A, pp. 1225–32.
24. W.R. Canon and O.D. Sherby: *Metall. Trans.*, 1970, vol. 1, pp. 1030–32.
25. F.A. Mohamed and T.G. Langdon: *Acta Metall.*, 1974, vol. 22, pp. 779–88.
26. S. Takeuchi and A.S. Argon: *J. Mater. Sci.*, 1976, vol. 11, pp. 1542–51.
27. W.C. Oliver and W.D. Nix: *Acta Metall.*, 1982, vol. 30, pp. 1335–47.
28. T.R. McNelley, D.J. Michel, and A. Salama: *Scripta Metall.*, 1989, vol. 23, pp. 1657–62.
29. I.C. Hsiao and J.C. Huang: *Metall. Mater. Trans. A*, 2002, vol. 33A, pp. 1373–84.
30. E.M. Taleff: in *Advances in Superplasticity and Superplastic Forming*, E.M. Taleff, P.A. Friedman, P.E. Krajewski, R.S. Mishra, and J.G. Schroth, eds., TMS, Warrendale, PA, 2004, pp. 85–94.
31. E.M. Taleff, G.A. Henshall, T.G. Nieh, D.R. Lesuer, and J. Wadsworth: *Metall. Mater. Trans. A*, 1998, vol. 29A, pp. 1081–91.
32. E.M. Taleff, P.J. Nevland, and P.E. Krajewski: *Metall. Mater. Trans. A*, 2001, vol. 32A, pp. 1119–30.
33. E.M. Taleff and J. Qiao: in *Light Metals 2001: Métaux Légers*, M. Sahoo and T. Lewis, eds., Canadian Institute of Mining, Metallurgy and Petroleum, Montreal, 2001, pp. 77–88.
34. T.S. Lundy and J.F. Murdoch: *J. Appl. Phys.*, 1962, vol. 33, pp. 1671–73.
35. D. Turnbull: *Trans. Am. Inst. Min. Metall. Eng.*, 1951, vol. 191, pp. 661–65.
36. H.J. Frost and M.F. Ashby: *Deformation Mechanism Maps*, Pergamon, Oxford, United Kingdom, 1982, p. 21.
37. G. Moreau, J.A. Cornet, and D. Calais: *J. Nucl. Mater.*, 1971, vol. 38, pp. 197–202.
38. S.J. Rothman, N.L. Peterson, L.J. Nowicki, and L.C. Rothman: *Phys. Status Solidi (B)*, 1974, vol. 63, pp. K29–K33.
39. L.F. Mondolfo: *Aluminum Alloys: Structure and Properties*, Butterworth and Co, London, 1976, p. 311.
40. M.A. Kulas, W.P. Green, E.M. Taleff, P.E. Krajewski, and T.R. McNelley: *Metall. Mater. Trans. A*, 2006, vol. 37A, pp. 645–55.
41. K. Oh-Ishi, J. Boydon, and T.R. McNelley: *J. Mater. Eng. Perform.*, 2004, vol. 13 (6), pp. 710–19.
42. M.T. Pérez-Prado, G. González-Doncel, O.A. Ruano, and T.R. McNelley: *Acta Mater.*, 2001, vol. 49, pp. 2259–68.
43. V. Randle and O. Engler: *Introduction to Texture Analysis: Macrotexture, Microtexture and Orientation Mapping*, Gordon and Breach, Amsterdam, 2000, pp. 127–33.
44. A.P. Zhilyaev, K. Oh-Ishi, G.I. Raab, and T.R. McNelley: *Mater. Sci. Eng.*, 2006, vol. A441, pp. 245–52.
45. J.H. Han and D.Y. Kim: *Acta Metall. Mater.*, 1995, vol. 43, pp. 3185–88.
46. M. Hatherley and W.B. Hutchinson: *An Introduction to Textures in Metals*, Chemeloeon Press, London, 1979, p. 11.
47. J.K. Mackenzie: *Biometrika*, 1958, vol. 45, pp. 229–40.

48. N. Gao, S.C. Wang, H.S. Ubhi, and M.J. Starink: *J. Mater. Sci.*, 2005, vol. 40, pp. 4971–74.
49. M.-A. Kulas, P.E. Krajewski, T.R. McNelley, and E.M. Taleff: in *Hot Deformation of Aluminum Alloys III*, Z. Jin, A. Beaudoin, T. Bieler, and B. Radhakrishnan, eds., TMS, Warrendale, PA, 2003, pp. 499–507.
50. M.A. Khaleel, H.M. Zbib, and E.A. Nyberg: *Int. J. Plast.*, 2001, vol. 17, pp. 277–96.
51. D.H. Bae and A.K. Ghosh: *Acta Mater.*, 2002, vol. 50, pp. 993–1009.
52. D.H. Bae and A.K. Ghosh: *Acta Mater.*, 2002, vol. 50, pp. 1011–29.
53. F.J. Humphreys: *Acta Metall.*, 1977, vol. 25, pp. 1323–44.
54. B.M. Watts, M.J. Stowell, B.L. Baike, and D.G.E. Owen: *Met. Sci. J.*, 1976, vol. 10 (6), pp. 189–97.
55. E. Hornbogen: *Metall. Trans. A*, 1979, vol. 10A, pp. 947–72.
56. R. Grimes: in *Superplasticity*, Lecture Series 168, NATO Advisory Group for Aerospace Research and Development (AGARD), Paris, 1988, pp. 8.1–8.16.
57. S.J. Hales and T.R. McNelley: *Acta Metall.*, 1988, vol. 36, pp. 1229–39.
58. F.J. Humphreys: *Acta Mater.*, 1997, vol. 45, pp. 4231–40.
59. R.D. Doherty, D.A. Hughes, F.J. Humphreys, J.J. Jonas D. Juul Jensen, M.E. Kassner, W.E. King, T.R. McNelley, H.J. McQueen, and R.D. Rollett: *Mater. Sci. Eng.*, 1997, vol. A238, pp. 219–74.
60. T.R. McNelley and M.E. McMahon: *Metall. Mater. Trans. A*, 1997, vol. 28A, pp. 1879–87.
61. M.T. Pérez-Prado, T.R. McNelley, O.A. Ruano, and G. González-Doncel: *Metall. Mater. Trans. A*, 1998, vol. 29A, pp. 485–92.
62. T.R. McNelley, M.E. McMahon, and M.T. Pérez-Prado: *Philos. Trans. R. Soc. A*, 1999, vol. 357, pp. 1683–1705.
63. T.R. McNelley, D.L. Swisher, and M.T. Pérez-Prado: *Metall. Mater. Trans. A*, 2002, vol. 33A, pp. 279–90.